Structural and electronic properties of C_{60}

N. Troullier and José Luís Martins
Department of Chemical Engineering and Materials Science, University of Minnesota, Minneapolis, Minnesota 55455
(Received 16 August 1991; revised manuscript received 10 March 1992)

We present pseudopotential local-density calculations of the electronic and structural properties of solid C_{60} (fullerite). The calculated molecular bond lengths, lattice constant, bulk modulus, enthalpy of formation, and the equation of state for compression are in good agreement with experiment. The shape of the theoretical density of states is in excellent agreement with the experimental photoemission and inverse photoemission spectra. We also present the calculated band structure for the states near the fundamental gap. We have made a thorough analysis of the electronic states of C_{60} and found that they can be conveniently classified according to their angular character, and use it to identify the origin of the peaks in the electronic density of states.

I. INTRODUCTION

In the mid-1980s a cluster containing 60 carbon atoms was observed to be exceptionally stable in a molecular beam.[1] It was proposed that the stability of this molecule, C_{60} fullerite, was due to a highly symmetric truncated icosahedral shape. With the recent breakthrough of Krätschmer *et al.*[2] the production of C_{60} in macroscopic amounts has been achieved, and a molecular solid formed by C_{60} molecules has been synthesized. Solid C_{60} is a new crystalline material that is expected to have different properties than the other two more common forms of crystalline carbon, diamond and graphite.

With the availability of macroscopic amounts of C_{60}, the basic properties of this molecular solid have been determined. The early evidence for the cage geometry[3] was confirmed and the icosahedral symmetry established from Raman[4] and NMR (Refs. 5–7) spectra. The molecular bond lengths have been obtained from NMR (Ref. 8) and x-ray-scattering[9,10] spectra. The compressability has been measured.[11] The phonon spectra were determined with Raman,[4,12] infrared,[13,12] and neutron-scattering[14] experiments. The electron spectra were observed with photoemission[15] and inverse photoemission.[16] The report of the formation of conducting films of C_{60} by alkali-metal doping[17] was quickly followed by the exciting discovery of superconductivity[18] in interstitially doped K_3C_{60} with a critical temperature of $T_c = 18$ K. Recently, superconductivity was observed in Rb_3C_{60},[19] Cs-doped C_{60},[20] and Cs_2RbC_{60},[21] with critical temperatures of $T_c = 28$, 30, and 33 K, respectively.

We have performed pseudopotential local-density calculations of the structural and electronic properties of solid C_{60}. The calculated molecular bond lengths (1.382 and 1.444 Å), lattice constant of fullerite (14.0 Å), and cohesive energy (1.6 eV per molecule) are in good agreement with experiment. The calculated pressure versus volume equation of state also agrees with the experimental data. The shape of the theoretical density of states is in excellent agreement with the measured photoemission and inverse photoemission spectra. We have calculated the band structure of fullerite, the band gap is direct at X and is 1.18 eV wide. The width of the lowest set of conduction bands is 0.47 eV. Because of the problems with the local-density approximation the true band gap should be larger. From our analysis of the wave functions we can classify them according to their σ and π character, and their dominant angular momentum component with respect to the center of the C_{60} molecules. We are able to classify the preeminent features of the density of states, and we show how approximate molecular orbitals with the correct symmetry can be written for the π system of the molecule. Similar calculations were done for K_nC_{60} crystals and will be discussed elsewhere.

In Sec. II we present an outline of the computational procedure. In Sec. III we discuss the calculated structural properties. The electronic structure is presented in Sec. IV, and in Sec. V we discuss the electron wave functions. Atomic units are used throughout this paper unless otherwise noted.

II. COMPUTATIONAL PROCEDURE

The electronic structure calculations for C_{60} were performed with the plane-wave pseudopotential local-density[22] method.[23,24] We use the Ceperley and Alder[25] form of exchange correlation, as parametrized by Perdew and Zunger.[26] The pseudopotentials were generated using a method proposed by us,[27] which has the advantage of producing "soft" pseudopotentials for first-row elements, such as carbon. The carbon pseudopotential used in these calculations was generated in the ground-state valence configuration $2s^22p^2$. The radial cutoffs, i.e., the radius at which inside this point the pseudo-wavefunctions are allowed to deviate from the all-electron wave functions, were $r_{cs}=r_{cp} = 1.50a_0$. We use the p pseudopotential as the local potential and neglect the nonlocality for the d and higher scattering channels. The carbon potential was then made separable using the procedure of Kleinman and Bylander.[28] We checked that

no spurious ghost states existed by using the theorem of Gonze, Käckell, and Scheffler[29] and by inspection of the logarithmic derivatives of the separated carbon pseudopotential.

The plane-wave basis used for these calculations has the advantage of being easy to use and has the nice mathematical properties of being a complete and orthogonal basis set. The convergence of the calculated properties when using plane waves can be checked by increasing the number of plane waves. In practice, we include all plane waves with a kinetic energy less than a chosen cutoff energy, $E_{\rm cut}$=49 Ry. With this particular cutoff energy, the total energy of all the carbon crystals (C_{60}-fullerite, graphite, and diamond) are converged to within 0.05 eV/atom.[27] This small energy correction was included in all the reported values of atomization energies. With the $E_{\rm cut}$ = 49 Ry cutoff energy, the number of plane waves used for the different calculations ranged from 17 000 to 110 000, depending on the unit-cell volume. In order to handle these extremely large matrices, highly efficient and robust iterative methods were used to diagonalize the Hamiltonian matrix.[30,31] This type of iterative procedure does not require the actual calculation and storage of the Hamiltonian matrix H, but only the resulting product $H\Psi$.[32] This task is accomplished by utilizing fast Fourier transforms and the dual-space method[30] to calculate the action of the kinetic-energy operator in momentum space and the local potential operator in real space.

Since the size of the Brillouin zone for solid C_{60} is small and the occupied electron states of the system are predominantly of molecular character, the band dispersion of the filled states is small. As an example, the calculated width of the band derived from the highest occupied molecular orbital is ~0.6 eV. Use of only the Γ point in sampling this small Brillouin zone to calculate the screening potential was sufficiently accurate to obtain pictures of the wave functions and charge densities. However, to determine the structural properties, the band structure, and density of states for solid C_{60}, we found that two special **k** points were required to calculate the screening potential.

III. STRUCTURAL PROPERTIES

The structure of a truncated icosahedral C_{60} molecule consists of 20 hexagons and 12 pentagons (see Fig. 1). The molecule has two different types of bonds: a bond shared by two hexagons edges, $A_1 - A_2$ in Fig. 1, and a bond shared by a pentagon and hexagon edge, $A_1 - A_3$ or equivalently $A_1 - A_4$ in Fig. 1. These two bonds are often called "double" and "single" carbon bonds, but they are both mainly aromatic in character. Figure 1 also shows the weak intermolecular bonding between C_{60} molecular units (dashed lines).

For the isolated C_{60} molecule, the two bond lengths are the only degrees of freedom of its equilibrium structure. In solid C_{60}, we have the added freedoms of determining the Bravais lattice, the orientation and number of molecular units within the primitive cell, and the distortions of the molecule due to the crystal field.

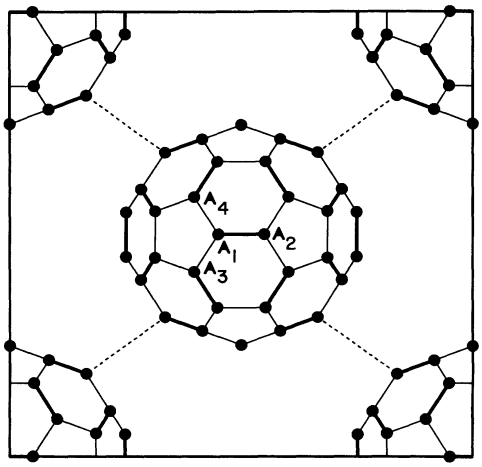

FIG. 1. Atomic positions of solid fcc-T_h^3 C_{60} projected on the (001) plane. The thick lines (e.g., from A_1 to A_2) show the "short" hexagon-hexagon edge bonds, and the thin lines (e.g., from A_1 to A_3 or from A_1 to A_4) show the "long" hexagon-pentagon edge bonds. The dashed lines represent the weak bonds between C_{60} molecules. The molecular units are orientated in the T_h^3 symmetry, maintaining the highest possible symmetry for the calculation.

In crystalline fullerite the C_{60} molecules are located at the sites of a face-centered-cubic (fcc) lattice.[9,33] This is consistent with a picture of weakly interacting, almost spherical molecules, that would like to form a closed-packed structure. Although the basic pattern is simple, the orientation of the C_{60} molecules raises some interesting questions. Below 249 K the C_{60} molecules are rotationally ordered and form a superstructure of the fcc lattice which has a simple-cubic lattice,[33] and the $Pa3$ space group[34] with four C_{60} molecules per primitive cell. In this low-temperature structure, the four C_{60} molecules are located at the unit-cell positions (0,0,0), (0,0.5,0.5), (0.5,0.5,0), and (0.5,0,0.5) and have different rotational orientations. Above 249 K fullerite has the a fcc crystal structure with orientational disorder.[33] We notice that the dynamics of this orientation order-disorder transition should be very interesting since the NMR data[35] finds such a transition well below 233 K, while above this temperature the spectra is consistent with a free rotation of the C_{60} molecules. We expect that further experimental work will identify whether the disordering is due to free rotation or to jumps of the molecules between equivalent orientations. First-principles molecular-dynamics calculations predicted a free rotation of the molecules.[36]

The existence of an orientational ordering transition show that the particular orientation of the molecules should not be important in determining the fundamental properties of fullerite. Since accurate calculations for the $Pa3$ structure with 240 atoms per unit cell would be too expensive, we performed our calculations for the simplest structure that has the molecules in a fcc lattice. We therefore placed the molecules in a fcc lattice and oriented them to obtain a tetrahedral space group

$T_h^3(Fm3)$ (see Fig. 1). This choice of the tetrahedral space group T_h^3 maintains the highest possible symmetry between the icosahedral symmetry of the C_{60} molecular units and the fcc lattice. With use of this type of arrangement, the difference between the experimental and theoretical structures is only in the weak bonds between molecules, and therefore our geometrical assumption is reasonable.

To obtain the optimized atomic positions for the fcc-T_h^3 C_{60} solid, we calculated the quantum-mechanical forces acting upon the atoms, and then adjusted the atomic positions using these forces, until the resulting forces were negligible. Several different initial starting configurations were used, in which the atoms were placed in the molecular icosahedral symmetry with different choices for the two C-C bond lengths. This procedure yielded two distinctly different types of C-C bonds. The calculated length of the shorter bond (hexagon-hexagon) was 1.382 Å and the longer bond (hexagon-pentagon) was 1.444 Å. While the influence of the tetrahedral crystal field does result in further distortions of these bonds, the effect is negligible and well below the accuracy of the calculation. These values are in good agreement with the x-ray data values of 1.391 Å for the shorter bond and 1.455 Å for the longer bond,[37] and also the NMR C^{13}-C^{13} values[8] of 1.40 ± 0.015 and 1.45±0.015 Å for the short and long bonds, respectively. Other calculations of the bond lengths in the solid found similar values of 1.40 and 1.45 Å for the short and long bonds using a pseudopotential plane-wave local-density approximation (LDA) method[36] and 1.39 and 1.45 Å using a Gaussian-orbital LDA method.[38] The most accurate calculations with correlated wave functions were done with the second-order Moller-Plesset (MP2) method and give bond lengths of[39] 1.406 and 1.446 Å. These are quite different from the large-scale Hartree-Fock[40] values of 1.369 and 1.453 Å, showing that inclusion of correlation (within the LDA or with correlated wave functions) is required to obtain the length difference between the short and long bonds that is in agreement with experiment. Among the molecular calculations of C_{60} bond lengths, we notice the following: Hučkel[41] gives 1.405 and 1.426 Å, Coulson-Golebiewski self-consistent Hučkel[42] gives 1.403 and 1.434 Å, MNDO (Ref. 43) gives 1.400 and 1.474 Å, self-consistent-field (SCF) STO-3G (Ref. 44) gives 1.376 and 1.465 Å, PRDDO (Ref. 45) gives 1.373 and 1.397 Å, semiempirical SCF molecular orbital (MO) (Ref. 46) gives 1.396 and 1.443 Å, PPP CI molecular orbital[47] gives 1.398 and 1.439 Å, INDO (Ref. 48) gives 1.397 and 1.449 Å, and LDA with Gaussians[49] gives 1.39 and 1.43 Å for the short and long C-C bonds in molecular C_{60}.

Compared to the length of the "single" C-C bond in diamond (1.544 Å) and organic molecules (~1.541 Å) the two bond lengths in C_{60} are both considerably shorter. The typical lengths of "double" C-C bond lengths in organic molecules are ~1.337 Å, making them much shorter then the C_{60} bonds. The in-plane C-C bonds found in graphite are 1.421 Å, and the bond lengths found for most aromatic compounds are ~1.395 Å, that is, they have the same order of magnitude as the bond lengths in C_{60}. This indicates that the bonding found in the C_{60} system has an aromatic character with a delocalized resonant π-bond system. This is confirmed by our calculated molecular orbitals as discussed in Sec. V.

TABLE I. Atomization energies E_{at} for C_{60} are listed for several lattice constants, a. The first two values were calculated using only the Γ point to sample the Brillouin zone, and the remaining values use two special **k** points to sample the Brillouin zone. The last eight values were used for the equation-of-state fitting in Table II.

a (Å)	E_{at} (eV)
22.033	-500.902 (Γ)
17.543	-501.761 (Γ)
14.875	-502.039
14.573	-502.106
14.235	-502.445
13.879	-502.267
13.614	-502.083
12.907	-498.239
12.381	-487.433
12.167	-480.185
12.022	-473.840

In Table I, we show the atomization energies E_{at} of fcc-T_h^3 C_{60} obtained for several lattice constants. These are obtained by subtracting from the total energy of the crystal, 60 times the calculated spin-polarized ground-state energy of the carbon atom. The values for the lattice constants range from 12.02 to 22.033 Å (~ 35% volume compression to ~ 300% volume expansion). For the two largest lattice constants (22.0 and 17.5 Å) we used only the Γ point to sample the Brillouin zone, the remaining values were obtained using two special **k** points. The data points (excluding the two largest lattice constants) were fitted to the Murnaghan,[50] the Birch-Murnaghan,[51] and the universal (by Vinet *et al.*)[52] equation of state. The best fit was obtained with the universal equation of state. In Table II we list the values obtained for the the equilibrium lattice constant a_0, the bulk modulus B_0, the pressure derivative of the bulk moduli B_0', and the enthalpy of formation H_f, for the three fits. Only in the case of the a_0=13.879 Å lattice constant were the internal degrees of freedom (the C_{60} bond lengths) optimized. For the expanded and contracted lattice constants, the geometric structure of the molecule was assumed to be the same as the one optimized at a_0=13.879 Å. We estimate from the calculated residual forces and force constants that the errors in the total energies are smaller than 0.7 mRy for the extreme case of the ~ 35% lattice volume compression. For all the other lattice constants the error estimates are even smaller in magnitude. We are therefore justified in neglecting further geometry optimization.

Compared to the value of the experimental lattice constant,[11] the calculated values are in very good agreement, being approximately 0.7–1.8 % smaller (see Table II). This slight underestimation of the lattice constant is typical of well-converged LDA plane-wave calculations. For the experimental lattice constant, the in-

TABLE II. The calculated equilibrium lattice constant a_0, the bulk modulus B_0, the pressure derivative of the bulk modulus B_0', and the enthalpy of formation H_f of C_{60} are compared with experiment (Ref. 11). The calculated values are from fits to the data listed in Table I using the equations of state of Murnaghan (Ref. 50), Birch-Murnaghan (Ref. 51), and the universal equation of state of Vinet *et al.* (Ref. 52). The enthalpy of formation is per carbon atom, and is referenced to the calculated total energy for carbon in the graphite structure. The positive values of H_f indicate that C_{60} is less stable than graphite.

	Murnaghan[a]	Birch-Murnaghan[b]	Universal[c]	Expt.[d]
a_0 (Å)	14.095	13.946	14.044	14.198
B_0 (GPa)	18.56	17.05	16.46	18.1 ± 1.8
B_0'	7.21	15.30	10.48	5.7 ± 0.6
H_f (eV)	0.388	0.391	0.389	

[a]Reference 50.
[b]Reference 51.
[c]Reference 52.
[d]Reference 11.

termolecular spacing between C_{60} centers is 10.040 Å. Given a molecular "diameter" of 7.047 Å obtained from the optimized bond lengths, this results in an intermolecular nearest carbon-carbon distance of 3.182 Å. This intermolecular carbon-carbon distance is slightly smaller than the 3.45-Å distance between graphite planes. This suggests that the bonding for the intermolecular nearest carbon-carbon atoms in C_{60} is slightly stronger than the interplaner graphite bonds. The calculated bulk modulus is also in good agreement with experiment (see Table II). The range of the calculated pressure derivatives of the bulk modulus is very large because this quantity is very sensitive to numerical noise and the choice of the fitted range of the lattice constant.

In Fig. 2, we plot the volumetric compression versus pressure for the fitted universal equation of state and the experimental data of Duclos *et al.*[11] The theoretical data have been normalized to the theoretical equilibrium volume. The agreement between the two curves is quite good, and demonstrates the rather large compressability of bulk fullerite, with a ~30% compression at 20 GPa. This large compressability is due to the relative softness of the intermolecular C-C bonds and not due to the compression of the basic C_{60} molecular units. (We recall that during compression with constant bond lengths the forces on the atoms remain small.)

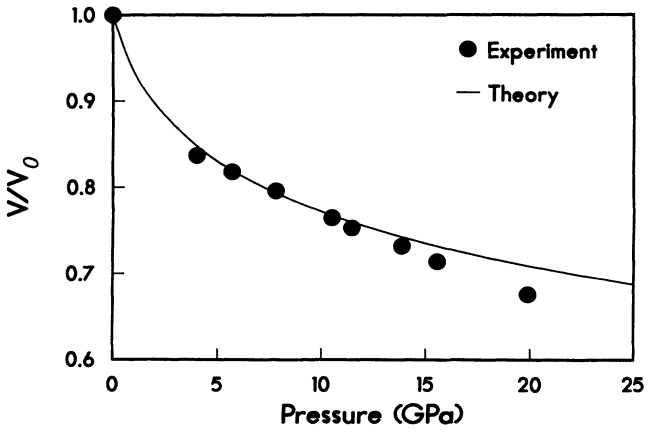

FIG. 2. Volume vs pressure equation of state for solid C_{60}. The solid line is from a fit to the calculated total energies as a function of lattice constant using the universal (Ref. 52) equation of state. The experimental data (large dots) are the room-temperature measurements of Duclos *et al.* (Ref. 11).

The last row of Table II lists the calculated enthalpies of formation per carbon atom, H_f, of C_{60}. The enthalpy of formation is referenced to the calculated total energy of carbon in the graphite structure using the same pseudopotential and plane-wave cutoff energy. The positive value of 0.4 eV for the enthalpy of formation shows that if the C-C bonds are broken, fullerite should transform into graphitic carbon. This is consistent with the fact that C_{60} is only formed in special circumstances. If we assume that for the lattice constant a=22.033 Å the intermolecular interaction is negligible, then we get a value for the cohesive energy of 1.6 eV per C_{60} molecule. (This is the energy required to remove one molecule from the fullerite crystal.) This compares quite well with the experimental[53] value of 1.739 ± 0.056 eV, and with the theoretical value of 1.6 eV from a calculation with a Gaussian basis set.[54] For a lattice constant of 22.033 Å, the C_{60} molecules are separated by 8.6 Å. Similar calculations for graphite have shown that when graphite planes are separated by 8.6 Å their interaction is very small in the local-density approximation.[55] Our value for the cohesive energy, while being strictly a lower bound, should therefore be quite close to the limit of infinite molecular separation.

IV. DENSITY OF STATES AND BAND STRUCTURE

We have calculated the band structure of C_{60} in detail for a lattice constant of 13.879 Å and for the fcc-T_h^3 geometry. The states at the center of the Brillouin zone (Γ) are shown in Table III. In that table we also give the

wave-function symmetry in the tetrahedral point group T_h. We have also classified the wave functions according to their σ or π character. As discussed in the next section, the σ and π orbitals have a dominant angular momentum contribution l when they are decomposed in spherical harmonics with respect to the center of the C_{60} molecule. We use that dominant angular momentum as a subscript in our labeling of the orbital type, as in σ_l and π_l.

In Fig. 3(a) we compare the theoretical results for the density of states (DOS) of the occupied orbitals to the photoemission data of Weaver *et al.*[15] for two different photon energies. The theoretical curve marked "DOS" in Fig. 3(a), was obtained by using the tetrahedron method with 64 **k** points in the Brillouin zone, which reduces to 8 points in the irreproducible wedge of the Brillouin zone. The curve was then convoluted with a Gaussian function of variable width, 0.23 eV + 0.02$|E|$. Here E is the energy measured in electron volts from the highest occupied state (which is at the X point of the Brillouin zone). The present DOS curve obtained with the tetrahedron method is nearly identical to that we obtained previously by using just the eigenvalues at the two special **k** points broadened by a similar Gaussian function.[15,56] Since the Brillouin zone is small, the **k**-space dispersion is also small, and the DOS is already well described by the use of just two **k** points. The series of curves shown at the bottom of Fig. 3(a) show the eigenvalues at Γ grouped according to their σ_l and π_l character and broadened with the same Gaussian procedure used for the DOS. It is clearly seen that orbitals of the same type are close in energy, that the bottom of the valence band is made of σ states, the top of π states, and that orbitals with increasing values of l have increasing energies.

In the DOS spectrum of Fig. 3(a) the peak at the top of the valence band is formed by π_5 states. This band is derived from the highest occupied molecular orbital, which has h_u symmetry. This level is split by the tetrahedral crystal field into a t_u and a e_u state at Γ and forms five dispersive bands. The π_5 DOS feature is followed by a π_4 peak at lower energy, which is derived from a g_g and a h_g molecular state. The π_4 states appear to be split in the Γ point curves, but in fact, they form a single broad feature in the DOS due to band dispersion effects. With increasing binding energy, we find the first feature with a mixture of σ and π character [labeled C in Fig. 3(a)]. This feature contains contributions from the σ_8', σ_9', and π_3 eigenstates, with the prime indicating the second peak of a split l state. This feature is somewhat narrower and more bound in experiment than in theory. We attribute this discrepancy to an underestimation of $\sim$ 0.5–1.0 eV in the binding energy for states containing

TABLE III. The energies of the electronic states at the point Γ in C_{60} are shown together with the wave-function symmetry in the tetrahedral space group, and the wave-function type (σ, π, etc., and the dominant angular momentum l) as described in the text. All energies are in eV, and are referenced to the highest occupied state at Γ.

Energy (eV)	Label	Energy (eV)	Label	Energy (eV)	Label
-18.766	σ_0-a_g	-7.109	σ_7-t_u	-0.965	π_4-t_g
-18.146	σ_1-t_u	-6.533	σ_7-t_u	-0.225	π_5-e_u
-17.262	σ_2-t_g	-5.829	σ_7-a_u	0.000	π_5-t_u
-17.221	σ_2-e_g	-5.802	σ_7-t_u	1.710	π_5-t_u
-16.098	σ_3-t_u	-5.563	π_1-t_u	2.372	π_6-t_g
-15.381	σ_3-a_u	-5.389	π_2-t_g	3.469	π_5-t_u
-15.326	σ_3-t_u	-5.371	σ_8-e_g	4.052	π_6-e_g
-14.137	σ_4-e_g	-5.257	σ_8-t_g	4.103	π_6-t_g
-13.983	σ_4-t_g	-5.004	π_2-e_g	4.217	C_0-a_g
-13.585	σ_4-a_g	-4.946	σ_8-a_g	4.971	π_7-e_u
-13.542	σ_4-t_g	-4.929	σ_8-t_g	5.149	π_6-a_g
-12.021	σ_5-e_u	-4.587	σ_8-t_g	5.515	π_7-t_u
-11.993	σ_5-t_u	-4.109	σ_9-t_u	5.878	σ_9-a_u
-11.873	σ_5-t_u	-4.089	σ_9-a_u	6.240	π_6-t_g
-10.917	σ_5-t_u	-3.597	π_3-a_u	6.423	σ_9-t_u
-9.830	σ_6-t_g	-3.452	π_3-t_u	6.495	O_0-a_g
-9.752	σ_6-e_g	-3.189	σ_8-e_g	6.974	T_{0A}-a_u
-9.564	σ_6-t_g	-3.120	σ_8-t_g	7.212	T_{0B}-a_g
-9.423	σ_6-a_g	-2.766	σ_9-e_u	7.430	C_1-t_u
-8.252	σ_6-a_g	-2.755	σ_9-t_u	7.454	σ_{10}-t_g
-8.128	σ_6-t_g	-2.628	π_3-t_u	7.815	σ_9-t_u
-7.368	σ_7-e_u	-1.850	π_4-e_g	8.298	C_2-t_g
-7.271	σ_7-t_u	-1.615	π_4-a_g	8.318	σ_{10}-e_g
-7.114	π_0-a_g	-1.084	π_4-t_g	8.754	O_1-t_u

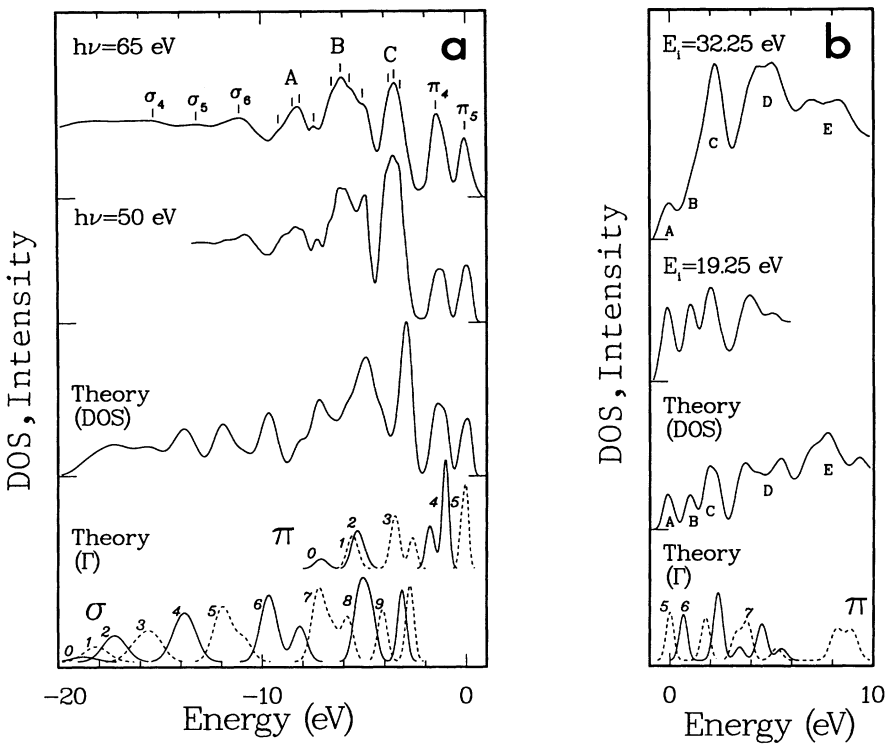

FIG. 3. In (a) we show the calculated density of states (DOS) spectrum for the valence states of solid C_{60}, and compare them to the experimental photoemission data of Weaver *et al.* (Ref. 15). The bottom curve in the figure shows the distribution of σ and π levels at the Γ point in the Brillouin zone. Each group is labeled with its appropriate angular momentum, l. All of the theoretical curves were Gaussian broadened for easier comparison to the experimental data. In (b) we show the lower conduction states in the same format as the valence states and compare them to the experimental inverse photoemission data of Jost *et al.* (Ref. 16). The theoretical conduction band DOS was also broaden to ease the comparison to experiment.

σ character with respect to states containing π character, as a result of using the local-density approximation. In fact, similar pseudopotential calculations for graphite[55] show a similar discrepancy with experiment in the position of the top of the σ band with respect to the highest occupied π state. Continuing down in energy, we see the broad feature labeled B in Fig. 3(a), which contains at least four features and is followed by a small peak. These features correspond to the σ_7', σ_8, σ_9, π_1, and π_2 states. The broad feature A appears to have at least three peaks, and shows the largest deviation between experiment and theory. It corresponds to the σ_6', σ_7, and π_0 theoretical states. The next three features correspond to the σ_4, σ_5, and σ_6 states. The lowest energy features would correspond to the remaining σ states.

In Fig. 3(b) we show the calculated density of states for the empty states of C_{60} and compare it to two sets of inverse photoemission data of Jost *et al.*[16] The density of states is obtained by the same Gaussian broadened tetrahedron method, with the change that now the energy is measured with respect to the bottom of the empty states (X point). This curve is again nearly identical to our previous results using only two **k** points.[16] The agreement between the theoretical DOS and the experimental data is excellent. At the bottom of the figure we show the contributions to the density of states at Γ from the σ and π states decomposed according to their dominant angular momentum.

For the conduction band, shown in Fig. 3(b), we have the lowest DOS feature, labeled A in Fig. 3(b), formed by a π_5 state which is derived from the lowest unoccupied molecular orbital of t_{1u} symmetry. The next peak (labeled B) is derived from a π_6 state. Notice that the B peak appears at lower energy in the Γ-point spectrum than in the two **k**-point density-of-states spectrum. Contributing to the third feature in the conduction band (C), we find the first nonmolecular state at 4.217 eV. This state is just ~0.42 eV above the self-consistent potential maximum, and has a wave function localized within the center of the C_{60} cage and of $l = 0$ character, which we label as C_0 (see Table III). From the examination of the self-consistent potential, we find that there exist relatively flat regions at the center of the molecular unit, and at the octahedral and tetrahedral interstitials. Wave functions localized near the octahedral and tetrahedral interstitial sites of the fcc lattice first appear at 4.8 eV and ~5.3 eV above the conduction-band minimum and are labeled O_0, T_{0A}, and T_{0B} in Table III. There are two equivalent tetrahedral interstitials, and the splitting between the bonding (T_{0B}) and antibonding (T_{0A}) states is ~0.24 eV. Two other features (D and E) appear in the inverse photoemission spectra, and they correspond

to prominent features in the theoretical density of states. These features contain contributions from a few π states, antibonding σ_9 states, and from the nonmolecular states which start the transition to the "delocalized" states expected for higher electron energies.

In both the photoemission and inverse photoemission spectra we can see numerous and sharp features, in particular near the top of the valence band and the bottom of the conduction band. The photoemission spectra of C_{60} have many more distinct and sharper features than either of the other two forms of crystalline carbon, diamond and graphite. This richness and sharpness of structures reflects the molecular character of solid C_{60}. For a detailed analysis of the experimental aspects of the photoemission and inverse photoemission spectra of C_{60} we refer the reader to the recent papers of Weaver and coworkers.[15,57,58] The densities of states for C_{60} calculated by other authors[36,54,59,60] using the local-density approximation are similar to our results, the small differences are due to numerical details, like the choice of the basis set.

In Fig. 4 we plot the band structure of C_{60} along the Δ symmetry direction (Γ-X), and the Z symmetry direction (X-W), for energies close to the fundamental gap, showing the highest group of valence bands and the two lowest groups of conduction bands. The gap is direct at X. The transverse and longitudinal effective masses for holes are 1.26 and 3.31, respectively. The transverse and longitudinal electron effective masses are 1.15 and 1.33. Our bands are quite different from the results of a local-density calculation with a Gaussian basis set.[54] For example, our top valence band is broader (0.58 versus 0.42 eV) and the gap is narrower (1.18 versus 1.5 eV). The details of the band dispersion are also different. The calculation with Gaussians used only two decays per orbital. Chelikowsky and Louie[61] have found that the use of two Gaussians per orbital for carbon will result in reasonable solid-state properties, but not in eigenvalues. In atomic calculations using the same pseudopotential and Gaussians decays as the Gaussian calculation we found errors of 2.5 and 3.5 eV in the atomic eigenvalues due to basis-set incompleteness. Our atomization energy for the C_{60} cluster of -8.3 eV per atom (see Table I) is lower (the cluster is more bound) than the -7.4-eV value of that Gaussian calculation,[54] but is in good agreement with the value of -8.51 eV of an all-electron calculation with a large Gaussian basis set.[62] We therefore attribute the disagreement between the two band structures to the very small basis set used in the Gaussian calculation. Our band structure is completely converged (within 1.4 meV) with respect to the number of plane waves.

As a closing comment about the band structure we noticed during the pressure studies that solid C_{60} undergoes a transition from a semiconductor state to a semimetal state at $\sim 35\%$ lattice compression. At this compression, corresponding to a pressure of 20–25 GPa, the Γ point of the conduction band coincides and then becomes lower than the valence-band maxima.

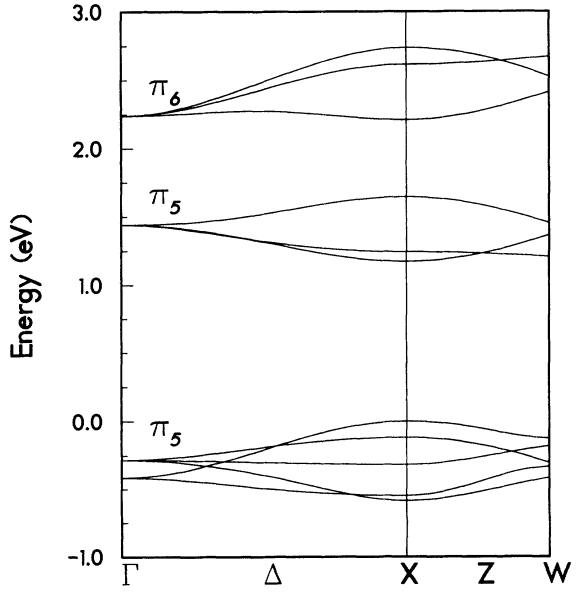

FIG. 4. The band structure of fcc-T_h^3 C_{60} along the Δ and Z directions is plotted for the highest valence bands and the two lowest conduction bands. The top of the valence band was chosen as the zero of the energy. The moderate dispersion of these levels clearly shows the departure from the molecular state.

V. WAVE-FUNCTION ANALYSIS

Making a drastic approximation we can assume that the potential of the isolated C_{60} molecule is an attractive spherically symmetric well. The bottom of this well occurs in a spherical surface with a radius of $\sim$3.55 Å and a width of $\sim$3.0 Å. In this model potential the electron states can be indexed with the quantum numbers, n, l, and m, where n is equal to one plus the number of radial nodes, and l is the angular momentum of the wave function. The model wave functions are the product of a radial function by a spherical harmonic Y_l^m. The real molecular potential is not spherically symmetric, but the pattern of the model and real molecular wave functions are quite similar for bound states, and the quantum numbers of the model can be used to label the true wave functions.[42,63–65] This labeling scheme can be put on a solid footing if we consider the topology of the nodal surfaces for the spherical model wave functions and for the C_{60} orbitals. For example, the σ-type molecular orbitals of C_{60} do not have a "radial" nodal surface in the wave functions and correspond to the $n = 1$ model wave functions, while the π molecular orbitals which have a radial nodal surface correspond to the $n = 2$ model functions. The radial nodal surface of the π orbitals of C_{60} is not a sphere, but rather a closed surface that resembles a dimpled ball with a diameter of $\sim$7 Å. In the absence of a symmetry plane the nodal topology of the wave functions allow us to keep the notation familiar to chemists for the delocalized three-dimensional orbitals of C_{60}. We should, however, remember that in the curved bonding network of C_{60} the π orbitals contain contributions from both $2s$ and $2p$ atomic orbitals.

A simple way to find the labels of the molecular wave functions is to calculate the auxiliary radial functions

$$F_l(r) = \sum_m \left| \int_{S_r} Y^*_{lm}(\mathbf{r})\psi(\mathbf{r})d\Omega \right|^2, \quad (1)$$

for each solid-state wave function ψ at the center of the Brillouin zone and for $l \geq 0$. The integration in Eq. (1) is carried out over the surface S_r of a sphere of radius r centered at the middle of the C_{60} cage. We then search among those functions to find which has the largest magnitude, $F_{l_0}(r)$, obtaining the angular label l_0, by inspecting the radial behavior of $F_{l_0}(r)$, we can easily determine the number of radial nodes, giving us the label n (and the σ, π, etc. character). Except for a few noticeable cases, each wave function of C_{60} has one particular function F_{l_0} that was at least one order of magnitude larger than the others, making the determination of n and l unambiguous. To give an explicit example of this procedure, we plot in Fig. 5 for several values of l the functions F_l for the highest occupied wave function at Γ. As can be seen in Fig. 5, the function F_5 is much larger then the F_3 or F_7 functions. Other functions F_l are even smaller for that orbital. A radial node in the wave function is responsible for the zero of F_5 in the plot. This indicates that the state has the labels of $n = 2$ and $l = 5$, and we call it a π_5 state.

In Fig. 6 we plot the angular deconvolution of the self-consistent potential via the use of Eq. (1) with the wave function replaced by the self-consistent potential. The functions for angular momentum $l = 0$ and $l = 10$ give the largest contributions. The largest contribution for $l < 10$ is for $l = 6$ and is almost two orders of magnitude smaller. There are no contributions from $l = 2$ and from odd values of l. The $l = 6$ and $l = 10$ components (allowed by the icosahedral symmetry) will respectively split all the wave functions with $l \geq 3$ and $l \geq 5$. The $l = 4$ contribution is due to the tetrahedral component of the crystal field and splits the wave functions with $l \geq 2$. Careful inspection of the eigenvalues of Table III or of Fig. 3 shows that the magnitude of the splittings within a shell reflect the magnitude of these angular components of the potential. For example, the large splitting of the π_5 eigenvalues (Fig. 3), which are important because they straddle the gap, is due to the large $l = 10$ component of the self-consistent potential.

To make our analogy with the spherical well model wave functions more rigorous we must consider the angular pattern of the nodes of the wave functions. To do this we cannot use the usual phase conventions of the spherical harmonics, but should use the linear combinations that transform according to the irreducible representations of the icosahedral point group. This is done in Table IV where we show the irreducible representations generated by the $2l + 1$ functions with angular momentum l, how these representations are further split by the tetrahedral field, and the combinations of spherical harmonic functions that are associated with those representations. For convenience the phases of the sine Y_{lsm} and cosine Y_{lcm} spherical harmonics of degenerate representations in Table IV were chosen such that the functions correspond to the irreducible representations of an orthorhombic point group with axes pointing in the x, y, and z directions.

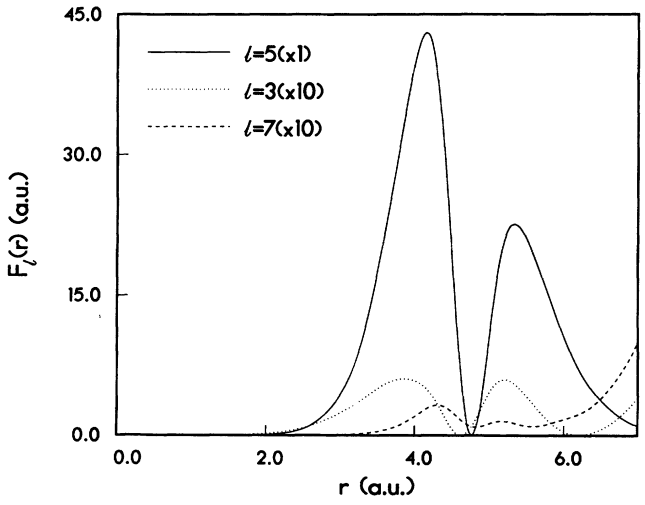

FIG. 5. The functions $F_l(r)$ [Eq. (2)] of the 120th wave function (highest valence band) are plotted for several values of the angular momentum l. The largest contribution is from the $l = 5$ component. The node in F_5 betrays a radial node in the wave function which is characteristic of π orbitals. From this deconvolution we can label unambiguously this wave function as π_5.

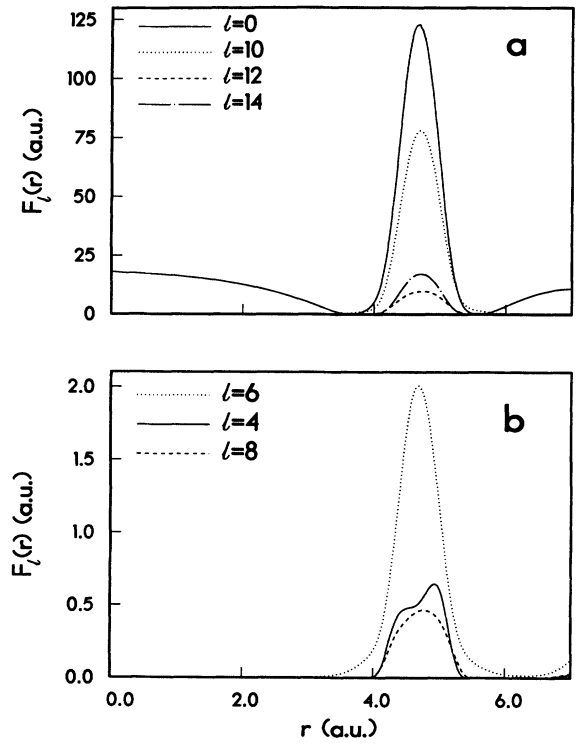

FIG. 6. The spherical deconvolution of the self-consistent potential plotted for several values of l. The icosahedral field contributes the $l = 6, 10, 12$ components.

TABLE IV. The table shows how the representations of the rotation group with $l \leq 9$ are split by the icosahedral point group I_h and how these are further split by the tetrahedral point group T_h. The fourth column lists the combinations of sine, Y_{lsm}, and cosine, Y_{lcm}, real spherical harmonics that generate those representations for $l \leq 6$.

l	I_h	T_h	I_{lm}
0	A_g	A_g	Y_{00}
1	T_{1u}	T_u	Y_{1c1}
			Y_{1s1}
			Y_{10}
2	H_g	E_g	Y_{2c2}
			Y_{20}
		T_g	Y_{2s2}
			Y_{2c1}
			Y_{2s1}
3	G_u	A_u	Y_{3s2}
		T_u	$0.500Y_{3c2} - 0.866Y_{30}$
			$0.991Y_{3c3} - 0.135Y_{3c1}$
			$0.926Y_{3s1} + 0.378Y_{3s3}$
	T_{2u}	T_u	$0.378Y_{3s1} - 0.926Y_{3s3}$
			$0.866Y_{3c2} + 0.500Y_{30}$
			$0.135Y_{3c3} + 0.991Y_{3c1}$
4	G_g	A_g	$0.645Y_{4c4} + 0.764Y_{40}$
		T_g	$0.874Y_{4s1} - 0.486Y_{4s3}$
			$0.764Y_{4s2} + 0.646Y_{4s4}$
			$0.943Y_{4c3} - 0.334Y_{4c1}$
	H_g	E_g	Y_{4c2}
			$0.764Y_{4c4} - 0.645Y_{40}$
		T_g	$0.334Y_{4c3} + 0.943Y_{4c1}$
			$0.486Y_{4s1} + 0.874Y_{4s3}$
			$0.646Y_{4s2} - 0.764Y_{4s4}$
5	T_{1u}	T_u	$0.523Y_{5c4} + 0.810Y_{5c2} - 0.265Y_{50}$
			$0.365Y_{5s1} + 0.803Y_{5s3} - 0.472Y_{5s5}$
			$0.637Y_{5c5} - 0.307Y_{5c3} - 0.707Y_{5c1}$
	T_{2u}	T_u	$0.927Y_{5s1} - 0.361Y_{5s3} + 0.101Y_{5s5}$
			$0.839Y_{5c4} - 0.433Y_{5c2} + 0.331Y_{50}$
			$0.694Y_{5c5} + 0.627Y_{5c3} + 0.354Y_{5c1}$
	H_u	E_u	$0.789Y_{5s2} + 0.614Y_{5s4}$
			$0.614Y_{5s2} - 0.789Y_{5s4}$
		T_u	$0.153Y_{5c4} - 0.395Y_{5c2} - 0.906Y_{50}$
			$0.334Y_{5c5} - 0.716Y_{5c3} + 0.612Y_{5c1}$
			$0.089Y_{5s1} + 0.474Y_{5s3} + 0.876Y_{5s5}$
6	A_g	A_g	$0.453Y_{6c6} - 0.548Y_{6c4} - 0.671Y_{6c2} + 0.207Y_{60}$
	T_{1g}	T_g	$0.316Y_{6s1} + 0.939Y_{6s3} + 0.135Y_{6s5}$
			$0.357Y_{6s2} + 0.585Y_{6s4} - 0.728Y_{6s6}$
			$0.557Y_{6c5} + 0.136Y_{6c3} - 0.820Y_{6c1}$
	G_g	A_g	$0.328Y_{6c6} + 0.758Y_{6c4} - 0.486Y_{6c2} - 0.286Y_{60}$
		T_g	$0.819Y_{6c5} - 0.253Y_{6c3} + 0.514Y_{6c1}$
			$0.620Y_{6s2} + 0.434Y_{6s4} + 0.654Y_{6s6}$
			$0.885Y_{6s1} + 0.343Y_{6s3} - 0.313Y_{6s5}$
	H_g	E_g	$0.829Y_{6c6} + 0.559Y_{6c2}$
			$0.354Y_{6c4} + 0.935Y_{60}$
		T_g	$0.700Y_{6s2} - 0.685Y_{6s4} - 0.207Y_{6s6}$
			$0.341Y_{6s1} + 0.020Y_{6s3} - 0.940Y_{6s5}$
			$0.137Y_{6c5} + 0.958Y_{6c3} + 0.252Y_{6c1}$
7	T_{1u}	T_u	
	T_{2u}	T_u	
	G_u	A_u	
		T_u	
	H_u	E_u	
		T_u	
8	T_{2g}	T_g	
	G_g	A_g	
		T_g	
	H_g	E_g	
		T_g	
	H_g	E_g	
		T_g	
9	T_{1u}	T_u	
	T_{2u}	T_u	
	G_u	A_u	
		T_u	
	G_u	A_u	
		T_u	
	H_u	E_u	
		T_u	

In Fig. 7 we compare the angular part of C_{60} wave functions with the icosahedral harmonics. These figures are contour plots in polar coordinates showing icosahedral harmonics and wave functions on the surface of a sphere of radius 3.17 Å, as a function of the azimuthal and polar angles. This is similar to a geographical map with the north pole at the midpoint between the atoms labeled A_1 and A_2 in Fig. 1. The large dots in Figs. 7(a) and 7(c) are the projection of the carbon-atom positions onto the spherical surface. The atom labeled A_1 in Fig. 1 is located at the top left in Figs. 7(a) and 7(c), with polar angle ~11.3° (latitude 78.7° north) and of azimuthal angle 0° (longitude). The radius used for Figs. 7(a) and 7(c) is just inside the sphere of the carbon atoms and was chosen to be near the maximum of the π wave functions (peaks of the $2p$ atomic orbitals). For σ states a radius of 3.5 Å would be more appropriate.

Figure 7(a) shows the angular plot for one of the wave functions derived from the h_{1u} highest occupied molecular orbital of C_{60}. It is a π_5 wave function of e_u symmetry in the tetrahedral point group of the solid. Figure 7(b) shows the spherical harmonic $0.789Y_{5s2}+0.614Y_{5s4}$ which can be associated with that state (Table IV). In Fig. 7(c) we show the angular plot for one of the degenerate wave functions derived from the t_{1u} lowest unoccupied molecular orbital of C_{60}. It is also part of a group of π_5 wave functions and has t_u symmetry in the solid. The corresponding spherical harmonic, $0.265Y_{50} - 0.810Y_{5c2} - 0.523Y_{5c4}$, is shown in Fig. 7(d). Comparing the two sets of figures we see an amazing similarity between the wave functions and the spherical harmonics. Of course, the C_{60} wave functions have added structure corresponding to the lobes of the $2p$ atomic functions which are on top of the carbon atoms; however, the nodal structure is clearly the same.

Using the similarity between wave functions and spher-

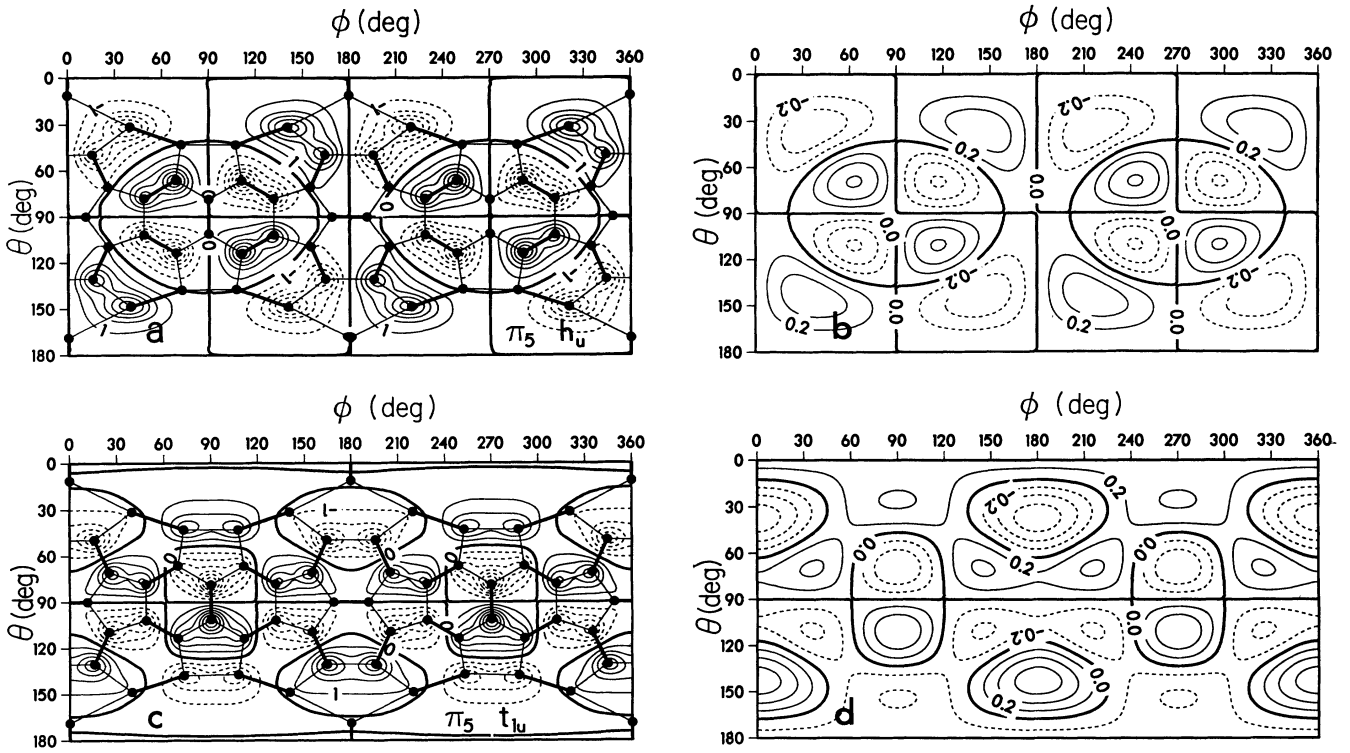

FIG. 7. Contour plots of the wave functions at Γ for states derived from the highest occupied (a) and lowest unoccupied (c) molecular orbitals of C_{60}. Corresponding icosahedral harmonics (see Table IV) are shown in (b) and (d). The wave functions are plotted at the surface of a sphere of radius of 3.17 Å, as a function of the azimuthal and polar angles (see text). The spacing of the contours is in a.u. The icosahedral harmonic plots (b) and (d) have been normalized to reflect the calculated wave functions. The dots and the straight lines are the projection of the carbon atoms of C_{60} onto the sphere and the bonding network, respectively. The similarities between the two types of functions is striking.

ical harmonics, we can write approximate π wave functions for C_{60} with the correct symmetry and correct shape without performing a single diagonalization. First, we form the atomic hybrid orbitals in the spirit of the π-orbital axis vector method.[41] These are obtained by requiring that three of the hybrid orbitals point in the direction of the three bonds around each carbon atom, and that all hybrids are normalized. For the atom labeled A_1 in Fig. 1 and with a z axis perpendicular to the plane of the figure, the dangling hybrid orbital is

$$\Phi_\pi(\mathbf{r}) \approx 0.2840\Psi_s(\mathbf{r}) - 0.2555\Psi_{px}(\mathbf{r}) + 0.9242\Psi_{pz}(\mathbf{r}). \tag{2}$$

We found that the s-p hybridization implied by the above expression agrees qualitatively with the calculated self-consistent wave functions. Approximate molecular π orbitals for C_{60} are then obtained by a linear combination of all Φ_π hybrid wave functions for the 60 carbon atoms, with coefficients given by the values taken at the atomic sites by the icosahedral harmonics listed in Table IV.

VI. CONCLUSIONS

Utilizing efficient diagonalization methods and "soft" pseudopotentials, we have used the plane-wave pseudopotential LDA method to accurately calculate the structural and electronic properties of solid fcc C_{60}. We have optimized the C_{60} structure and obtained values that are in excellent agreement with experiment for the bond lengths, the lattice constant, the equation of state for compression, and the cohesive energy. We have presented details of the density-of-states spectrum of fcc-C_{60}, which are in excellent agreement with experimental photoemission and inverse photoemission data. We have also presented the band structure of the highest valence band and the two lowest conduction bands, and we have listed values for the relevant longitudinal and transverse effective band masses. Using a simple labeling procedure, we have identified the preeminent features in the density-of-states spectrum. We have shown how these labels relate to the spherical harmonics, and have compared the angular behavior of the calculated wave functions with icosahedral sherical harmonics.

ACKNOWLEDGMENTS

We are grateful to J. H. Weaver, J. R. Chelikowsky, and R. E. Smalley for stimulating discussions and to P. J. Benning, M. B. Jost, and D. M. Poirier for helpful comments and suggestions. This work was supported by the Petroleum Research Fund of the American Chemical Society and by a computer time grant from the Minnesota Supercomputer Institute.

[1]H. W. Kroto, J. R. Heath, S. C. O'Brian, R. F. Curl, and R. E. Smalley, Nature (London) **318**, 162 (1985).
[2]W. Krätschmer, L. D. Lamb, K. Fostiropoulos, and D. R. Huffman, Nature (London) **347**, 354 (1990).
[3]F. D. Weiss, S. C. O'Brien, J. L. Elkind, R. F. Curl, and R. E. Smalley, J. Am. Chem. Soc. **110**, 4464 (1990).
[4]D. S. Bethune, G. Meijer, W. C. Tang, and H. J. Rosen, Chem. Phys. Lett. **174**, 219 (1990).
[5]R. D. Johnson, G. Meijer, and D. S. Bethune, J. Am. Chem. Soc. **112**, 8983 (1990).
[6]R. Taylor, J. P. Hare, A. K. Abdul-Sada, and H. W. Kroto, J. Chem. Soc. Chem. Commun. **20**, 1423 (1990).
[7]H. Ajie *et al.*, J. Phys. Chem. **94**, 8634 (1990).
[8]C. S. Yannoni, R. P. Bernier, D. S. Bethune, G. Meijer, and J. R. Salem, J. Am. Chem. Soc. **113**, 3190 (1991).
[9]R. M. Flemming, T. Siegrist, P. M. March, B. Hessen, A. R. Kortan, D. W. Murphy, R. C. Haddon, R. Tycko, G. Dabbagh, A. M. Mujsce, M. L Kaplan, and S. M. Zahurak, in *Clusters and Cluster-Assembled Materials*, edited by R. S. Auerback, J. Bernholc, and D. L. Nelson, MRS Symposium Proceedings No. 206 (Materials Research Society, Pittsburgh, 1991), p. 691.
[10]J. H. Hawkins, A. Meyer, T. A. Lewis, S. Loren, and F. J. Hollander, Science **252**, 312 (1991).
[11]S. J. Duclos, K. Brister, R. C. Haddon, A. R. Kortan, and F. A. Thiel, Nature (London) **351**, 380 (1991).
[12]D. S. Bethune *et al.*, Chem. Phys. Lett. **179**, 181 (1991).
[13]C. I. Frum, R. Engleman, Jr., H. G. Hedderich, P. F. Bernath, L. D. Lamb, and D. S. Bethune, Chem. Phys. Lett. **176**, 504 (1991).
[14]R. L. Cappelletti, J. R. D. Copley, W. A. Kamitakahara, F. Li, J. S. Lannin, and D. Ramage, Phys. Rev. Lett. **66**, 3261 (1991).
[15]J. H. Weaver, J. L. Martins, T. Komeda, Y. Chen, T. R. Ohno, G. H. Kroll, N. Troullier, R. E. Haufler, and R. E. Smalley, Phys. Rev. Lett. **66**, 1741 (1991).
[16]M. B. Jost, N. Troullier, D. M. Poirier, J. L. Martins, and J. H. Weaver, Phys. Rev. B **44**, 1996 (1991).
[17]R. C. Haddon *et al.*, Nature (London) **350**, 320 (1991).
[18]A. F. Hebard *et al.*, Nature (London) **350**, 600 (1991).
[19]M. J. Rosseinsky, A. P. Ramirez, S. H. Glarum, D. W. Murphy, R. C. Haddon, A. F. Hebard, T. T. M. Palstra, A. R. Kortan, S. M. Zahurak, and A. V. Makhija, Phys. Rev. Lett. **66**, 2830 (1991).
[20]S. P. Kelty, C.-C. Chen, and C. M. Lieber, Nature (London) **352**, 223 (1991).
[21]K. Tanigaki *et al.*, Nature (London) **352**, 222 (1991).
[22]P. Hohenberg and W. Kohn, Phys. Rev. **136**, B864 (1964); W. Kohn and L. J. Sham, *ibid.* **140**, A1133 (1965).
[23]J. Ihm, A. Zunger, and M. L. Cohen, J. Phys. C **12**, 4409 (1979).
[24]A general review of the LDA pseudopotential method has been done by W. E. Pickett, Comput. Phys. Rep. **9**, 117 (1989).
[25]D. M. Ceperley and B. J. Alder, Phys. Rev. Lett. **45**, 566 (1980).
[26]J. P. Perdew and A. Zunger, Phys. Rev. B **23**, 5048 (1981).
[27]N. Troullier and J. L. Martins, Phys. Rev. B **43**, 1993 (1991).
[28]L. Kleinman and D. M. Bylander, Phys. Rev. Lett. **48**, 1425 (1982).
[29]X. Gonze, P. Käckell, and M. Scheffler, Phys. Rev. B **41**, 12 264 (1990).
[30]J. L. Martins and M. L. Cohen, Phys. Rev. B **37**, 6134 (1988).
[31]J. L. Martins, N. Troullier, and S.-H. Wei, Phys. Rev. B **43**, 2213 (1991).
[32]R. Car and M. Parrinello, Phys. Rev. Lett. **55**, 2471 (1985).
[33]P. A. Heiney, J. E. Fischer, A. R. McGhie, W. J. Romanow, A. M. Denenstein, J. P. McCauley, Jr., A. B. Smith III, and D. E. Cox, Phys. Rev. Lett. **66**, 2911 (1991).
[34]R. Sachidanandam, A. B. Harris, P. A. Heiney, J. E. Fischer, and D. E. Cox (unpublished).
[35]C. S. Yannoni, R. D. Johnson, G. Meijer, D. S.Bethune, and J. R. Salem, J. Phys. Chem. **95**, 9 (1991).
[36]Q.-M. Zhang, J.-Y. Yi, and J. Bernholc, Phys. Rev. Lett. **66**, 2633 (1991).
[37]W. I. F. David *et al.*, Nature (London) **353**, 147 (1991).
[38]B. I. Dunlap, D. W. Brenner, J. W. Mintmire, R. C. Mowrey, and C. T. White, J. Phys. Chem. **95**, 5763 (1991).
[39]M. Haser, J. Almlöf, and G. E. Scuseria, Chem. Phys. Lett. **181**, 497 (1991).
[40]H. P. Lüthi and J. Almlöf, Chem. Phys. Lett. **135**, 357 (1987).
[41]See R. C. Haddon, L. E. Brus, and K. Raghavachari, Chem. Phys. Lett. **125**, 459 (1986).
[42]M. Ozaki and A. Takahashi, Chem. Phys. Lett. **127**, 242 (1986).
[43]M. D. Newton and R. E. Stanton, J. Am. Chem. Soc. **108**, 2469 (1986).
[44]R. L. Disch and M. Schulman, Chem. Phys. Lett. **125**, 456 (1986).
[45]D. S. Marynick and S. Estreicher, Chem. Phys. Lett. **132**, 383 (1986).
[46]M. Kataoka and T. Nakajima, Tetrahedron **42**, 6437 (1986).
[47]I. László and L. Udvardi, Chem. Phys. Lett. **136**, 418 (1987).
[48]T. Shibuya and M. Yoshitani, Chem. Phys. Lett. **137**, 13 (1987).
[49]B. I. Dunlap, Int. J. Quantum Chem. Symp. **22**, 257 (1988).
[50]F. D. Murnaghan, Proc. Natl. Acad. Sci. **30**, 244 (1944).
[51]F. Birch, J. Geophys. Res. **57**, 227 (1952).
[52]P. Vinet, J. Ferrante, J. R. Smith, and J. H. Rose, J. Phys.: Solid State Phys. **19**, L467 (1986); P. Vinet, J. Ferrante, J. H. Rose, and J. R. Smith, J. Geophys. Res. **92**, 9319 (1987); P. Vinet, J. H. Rose, and J. R. Smith, J. Phys. Condens. Matter **1**, 1941 (1989).
[53]C. Pan, M. P. Sampson, Y. Chai, R. H. Hauge, and J. L. Margrave, J. Phys. Chem. **95**, 2944 (1991).
[54]S. Saito and A. Oshiyama, Phys. Rev. Lett. **66**, 2637 (1991).
[55]M. C. Schabel and J. L. Martins (unpublished).
[56]J. L. Martins, N. Troullier, and J. H. Weaver, Chem. Phys. Lett. **180**, 457 (1991).
[57]P. J. Benning, D. M. Poirier, N. Troullier, J. L. Martins, J. H. Weaver, R. E. Haufler, L. P. F. Chibante, and R. E. Smalley, Phys. Rev. B **44**, 1962 (1991).
[58]P. J. Benning, D. M. Poirier, T. R. Ohno, Y. Chen, G. H. Kroll, M. B. Jost, F. Stepniak, J. H. Weaver, J. Fure, and R. E. Smalley, Phys. Rev. B **45**, 6899 (1992).
[59]J. W. Mintmire, B. I. Dunlap, D. W. Brenner, R. C. Mowrey, and C. T. White, Phys. Rev. B **43**, 14 281 (1991).
[60]B. P. Feuston, W. Andreoni, M. Parrinello, and E. Clementi, Phys. Rev. B **44**, 4056 (1991).
[61]J. R. Chelikowsky and S. G. Louie, Phys. Rev. B **29**, 3470

(1984).
[62]B. I. Dunlap *et al.*, J. Phys. Chem. **95**, 8737 (1991).
[63]J. L. Martins, N. Troullier, and J. H. Weaver, Chem. Phys. Lett. **180**, 457 (1991).
[64]P. W. Fowler and J. Woolrich, Chem. Phys. Lett. **127**, 78 (1986).
[65]A. J. Stone, Mol. Phys. **41**, 1339 (1980); A. J. Stone, Inorg. Chem. **20**, 563 (1984); A. J. Stone, Polyhedron **3**, 1299 (1984).